J. Fluid Mech. (1994), *vol.* 268, *pp.* 293–313

A new roll-type instability in an oscillating fluid plane

By EDWARD W. BOLTON[1,2] AND J. MAURER[2]

[1] Department of Geology and Geophysics, Yale University, PO Box 208109, New Haven, CT 06520-8109, USA

[2] Département de Physique, Ecole Normale Supérieure, 24 rue Lhomond, 75231 Paris Cédex 05, France

(Received 21 July 1992 and in revised form 1 December 1993)

A new roll-type instability has been discovered experimentally. When fluid between two closely spaced, parallel plates is oscillated about an axis midway between the plates, it exhibits an instability that takes the form of longitudinal rolls aligned perpendicular to the axis of rotation. The basic-state oscillatory shear flow, before the onset of rolls, may be viewed as driven by the $\dot{\Omega} \times \hat{r}$ term of the Navier–Stokes equation in the oscillatory reference frame. A regime diagram is presented in a parameter space defined by the maximum amplitude of angular oscillation, α, and the non-dimensional frequency, $\Phi = \omega d^2/\nu$. The equilibrium wavelength of the rolls scales with d, the gap spacing between the plates, and it increases as Φ increases. Supercritical to a weak-roll onset, an abrupt transition to stronger roll amplitude occurs. Photographs of the cell after an impulsive start show the roll development and initial increase in roll wavelength. A variety of phenomena are observed, including wavelength selection via defect creation and elimination, front propagation, secondary wave instabilities, and the transition to turbulence. We also present solutions of the Navier–Stokes equation for the basic-state shear flow in a near-axis approximation. We develop a simple resonance model which shows some promise in understanding the low-α, high-Φ behaviour of strong rolls. A theoretical analysis of this instability is presented by Hall (1994).

1. Introduction

We present the experimental results of a roll-type instability in an oscillating fluid plane. The basic-state shear flow is oscillatory in nature, and is independent of the coordinate in the direction of the rotational axis, except near the boundaries. Near the axis of rotation, the basic-state shear appears to be nearly independent of streamwise location. The cell geometry and the coordinate system are described in detail after the introduction. We observed roll formation with the roll-axis orientation perpendicular to the rotational axis, and parallel to the basic-state flow. Typical features of instabilities were observed, including secondary wave instabilities, and a transition to chaos. We also note that this instability may have industrial mixing applications.

The initial bifurcations observed in this study are similar to many of the classic instabilities of contained flows, such as Rayleigh–Bénard convection, Taylor–Couette flow, and roll formation from flow in curved channels. For the experiment reported here, the basic-state shear, before the onset of rolls, is periodic in time, with zero-mean flow. For an introductory treatment of periodically forced flows, see Drazin & Reid

(1981, §48). This subject has been reviewed by Davis (1976). Hall (1994) has recently performed a linear stability analysis of the basic-state flow relevant to our study.

In addition to the work on Taylor–Couette flow as discussed by Davis (1976), the torsional oscillation of an immersed cylinder also gives rise to Taylor vortices, as studied experimentally by Park, Barenghi & Donnelly (1980), and theoretically by Seminara & Hall (1976) and Hall (1981). The classic problem of oscillatory (flat) Stokes layers continues to be studied theoretically (Kerczek & Davis 1974; Hall 1978). More recent experimental and numerical work on Stokes layers (Akhavan, Kamm & Shapiro 1991*a*, *b*) provides insight into how a direct transition to turbulence occurs by secondary instabilities of a transient state.

A number of theoretical and experimental papers have addressed the influence of rotation on flows through straight ducts and channels. These 'flow through' studies lack the midplane inflexion point, the oscillatory forcing and the zero-mean flow characteristics of the present study, but exhibit many common features of the initial bifurcations. When the rotational axis is perpendicular to the direction of the basic-state mean flow, rolls appear, which are aligned in the flow direction (Hart 1971; Lezius & Johnston 1976; Speziale 1982; Kheshgi & Scriven 1985). For larger aspect ratio systems, multiple rolls were observed by Alfredsson & Persson (1989). They also observed secondary wavy instabilities and turbulence with coherent roll structure.

The sections to follow are organized in the following manner. In §2, we describe the experimental apparatus and methods. The experimental results of §3 begin with a discussion of the observed equilibrium flow regimes, which include the basic-state shear, the onset of weak rolls, the onset of strong rolls, secondary wavy instabilities, and turbulent flow within coherent roll structure. We then describe the wavelengths observed as equilibrium states. We also discuss the evolution of structures following an impulsive start of cell oscillations. In §4, we discuss the basic-state shear flow present before the onset of rolls. Our attention is focused on a 'near-axis approximation', where the basic-state velocity profile is assumed to be dependent only upon time and the coordinate position across the fluid gap. Low- and high-frequency limits are developed for the maximum velocity, and its location and phase. We then develop a simple resonance model in an attempt to understand the strong-roll onset for high forcing frequencies. In §5, we discuss some possible causes for the difference between weak and strong rolls. We also discuss relationships to other studies, and suggest some extensions of this study. This is followed by concluding remarks in §6.

2. Experimental apparatus and method

2.1. *Cell geometry*

We shall often refer to the coordinate system as defined here. The z-axis is vertical, parallel to the (oscillatory) rotational axis. The y-axis is across the gap, and the horizontal x-axis is in the fluid midplane (see figure 1*a*). The unit vectors $\{\hat{\imath},\hat{\jmath},\hat{k}\}$ point in the $\{x,y,z\}$ directions. The boundaries of the cell are at $x = \pm\frac{1}{2}L_x$, $y = \pm\frac{1}{2}d$, and $z = \pm\frac{1}{2}L_z$. The gap spacing d is the most important dimension, at least for the aspect ratios which have been investigated in this study. $\Omega(t)$ is the time-dependent angular velocity ($\boldsymbol{\Omega} = \Omega\hat{k}$). The instantaneous angle of the cell from its mean position in the fixed laboratory frame is dominantly $\theta = -\alpha\cos(\omega t)$, which implies that $\Omega = \alpha\omega\sin(\omega t)$. The presence of smaller-amplitude higher harmonics is discussed below. Dimensional analysis reveals that the following non-dimensional groups govern such flows forced by a single frequency: the amplitude of angular oscillation α; a non-dimensional frequency $\Phi = \omega d^2/\nu$, where ν is the kinematic viscosity; and the

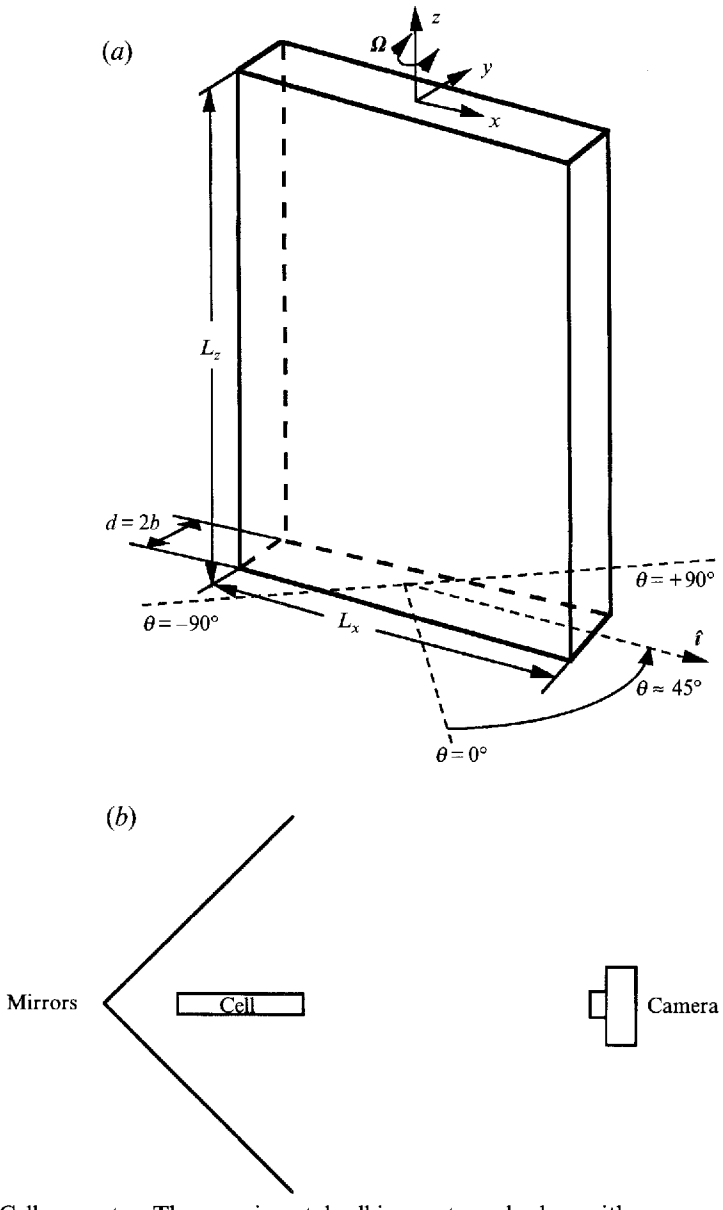

FIGURE 1. (*a*) Cell geometry. The experimental cell is a rectangular box with gap spacing d, height L_z, and width L_x. It oscillates about a vertical axis in the fluid midplane. For pure harmonic forcing, the instantaneous position of $\hat{\imath}$ in the oscillating frame of the cell is oriented at an angle $\theta = -\alpha\cos(\omega t)$ with respect to the cell's mean position in the fixed frame at $\theta = 0$. In this perspective view, the cell is at $\theta \approx 45°$, and oscillates up to $\theta = \pm\alpha = \pm 90°$. The angular velocity of the cell is $\boldsymbol{\Omega} = \Omega(t)\hat{\boldsymbol{k}}$, with $\Omega(t) = \alpha\omega\sin(\omega t)$. (*b*) The arrangement of the mirrors, cell and camera (as looking down from above) used for the creation of figure 2(*a–c*).

horizontal and vertical aspect ratios: $A_x = L_x/d$ and $A_z = L_z/d$. For the cells (table 1) and fluids used in this study, we found no resolvable dependence of the equilibrium states upon the aspect ratios. The time-dependent evolution after an impulsive start was studied only for a single aspect ratio. We note that the phenomenon of roll onset does not depend upon the orientation of the z-axis with respect to gravity. We also emphasize that the roll axes are perpendicular to the rotational axis. The roll

Cell	d (cm) $+0.02, -0$	L (cm) ± 0.05	l (cm) ± 0.05	A_L	A_l	A_L/A_l
1	0.80	27.7	18.0	34.62	22.50	1.54
2	0.80	27.6	17.5	34.5	21.88	1.58
3	0.50	35.0	22.5	70.0	45.0	1.56
4	0.50	17.5	11.25	35.0	22.5	1.56
5	0.25	8.75	5.63	35.0	22.52	1.56

TABLE 1. The interior dimensions of the five cells used for this experiment. The gap spacing of the cell is d, the length is L, and the width is l (error estimates for these are given at the top). Most of the experiments were performed with $L_z = L$, $L_x = l$ (cf. figure 1). However, we also did some runs with the alternate orientation, i.e. with $L_x = L$, $L_z = l$. The flow regime appeared insensitive to such changes in orientation to within the resolution attainable. The aspect ratios are $A_L = L/d$, $A_l = l/d$. All of the cells had similar values of A_L/A_l.

orientation in this experiment is then similar to that of Taylor–Couette rolls, i.e. parallel to the direction of the basic-state velocity, rather than perpendicular to the flow as is the case for the Kelvin–Helmholtz instability.

2.2. *The apparatus*

The cells were made of two glass plates, separated by square-section bars near the edges. The perimeter was sealed with glue. Fluids were introduced through a small hole between the spacer bars, which could later be sealed. The dimensions of the space for the fluid are defined in figure 1(*a*). The various cells used in the experiments are listed in table 1. Above the motor and linkage, a metal channel supporting a frame was bolted to the cell-axis shaft (which oscillated during experimental runs). The cell was secured to the metal frame, with the line of the rotational axis in the fluid midplane. On the lower edge of the metal channel, a pointer indicated the angular position on a circular protractor centred at the cell axis. A variable-speed motor supplied oscillation frequencies between 0 and 2 Hz.

The cell was connected to the motor via a cam linkage. We calculated the cell position, relative to an arbitrary reference angle, over a single rotation of the cam. Fourier analysis of this result revealed the amplitude and phase of the higher harmonics, relative to the fundamental frequency ($f = \omega/(2\pi)$). The results indicate that the first overtone ($2f$) had an amplitude between 2 and 5% of the fundamental frequency, with the larger contributions coming from larger α. The next overtone ($3f$) had an amplitude between 0.5 and 2% of the fundamental frequency. Higher harmonics had smaller amplitudes, all less than 0.5%.

2.3. *Fluids utilized*

Distilled water was the experimental fluid for most of the trials. The flow was visualized with a 3–5% addition of Kalliroscope solution (AQ-1000), making the particulate concentration up to about 0.03%. Onset values for strong rolls (described below) were also determined with acetone as the fluid, and similar Kalliroscope concentrations. The material properties of water were taken from Weast (1971) and those of acetone were taken from Washburn (1928). The phenomena described in this paper are not driven by the density difference of the visualization particles and the fluids. This was verified by observing the dynamics of a test cell containing a solution of Freon TF with a small addition of Kalliroscope PF-1000 concentrate, where the particles have the same density as the fluid.

2.4. *Experimental method*

An experimental run with an impulsive start proceeded as follows. A voltage level for the motor was selected, determining the frequency, and the angle α set. The frequency of cell oscillation was determined by timing 10–20 cycles with a stop-watch. After allowing the cell to rest until fluid motion ceased, oscillations were resumed. After a number of cycles, the oscillation was stopped and the structure of the flow was observed and classified. If present, rolls or roll pairs were counted over a measured vertical distance. Many repetitions of the above procedure at different stopping times then provided distributions of wavelength data similar to figure 5 (although that figure was taken from photographs described below). Allowing the cell to oscillate for many cycles, until the pattern seemed to be in equilibrium, provided data for the regime diagram (figure 3) and the equilibrium wavelengths (figure 4). Figures 3–5 are discussed further in the results section below.

Photographs taken every few cycles, after an impulsive start, provided data such as the wavelength evolution (figure 5) and the time-dependent flow regimes (figure 2). Two mirrors were placed at right angles on a platform around the cell. The cell was arranged to have an extremum of the angle θ while the x-axis was in line with the vertex of the mirrors on one side and the camera on the other (as illustrated in figure 1*b*). The photographs show an edge of the cell between the mirrors, and opposite faces of the cell on each mirror. The cell faces near the edge closest to the camera appear on the left and right edges (of each part (i–iv)) of the photographs in figure 2(*a–c*). Slight errors in timing the moment of the photographs, in addition to slight mirror tilts, led to linear trends in the translation of distances on photographic prints to distances on the cell. We corrected for these trends during the wavelength measurements.

2.5. *Error estimates*

We estimate the experimental errors as follows. The gap spacing d, as reported in table 1, could have an error of $(+0.02, -0)$ cm. The angle α was accurate to within $\pm 1°$. The measured frequency was accurate to within 1%. We recorded temperatures between 20 °C and 26 °C, with a mean of 23 °C. The visual observations of onset of weak and strong rolls were difficult, and were somewhat dependent upon both the observer and the illumination, contributing a possible error of ± 10 in Φ_{onset}. The axis of rotation was in the fluid midplane to within ± 0.05 cm, and was vertical to within 1°. In fact, the onset of rolls appears to be insensitive to large changes in the axis position, provided that the axis is parallel to the fluid midplane and a cell edge. With all uncertainties included, the maximum discrepancy between values of Φ_{onset} of weak or strong rolls (discussed in §3) from various observations is on the order of $\Delta\Phi \approx 20$, for $\Phi \leqslant 100$. An improved experimental design would include better temperature control and quantitative roll velocity measurements.

3. Experimental results

3.1. *Flow states observed*

Several regimes of flow patterns were observed visually. We shall first discuss the regimes which persist as equilibrium states. The results for the onset of rolls were independent of the aspect ratios of the cells within the resolution attainable. Later we shall discuss the pattern evolution after an impulsive start from a rest state.

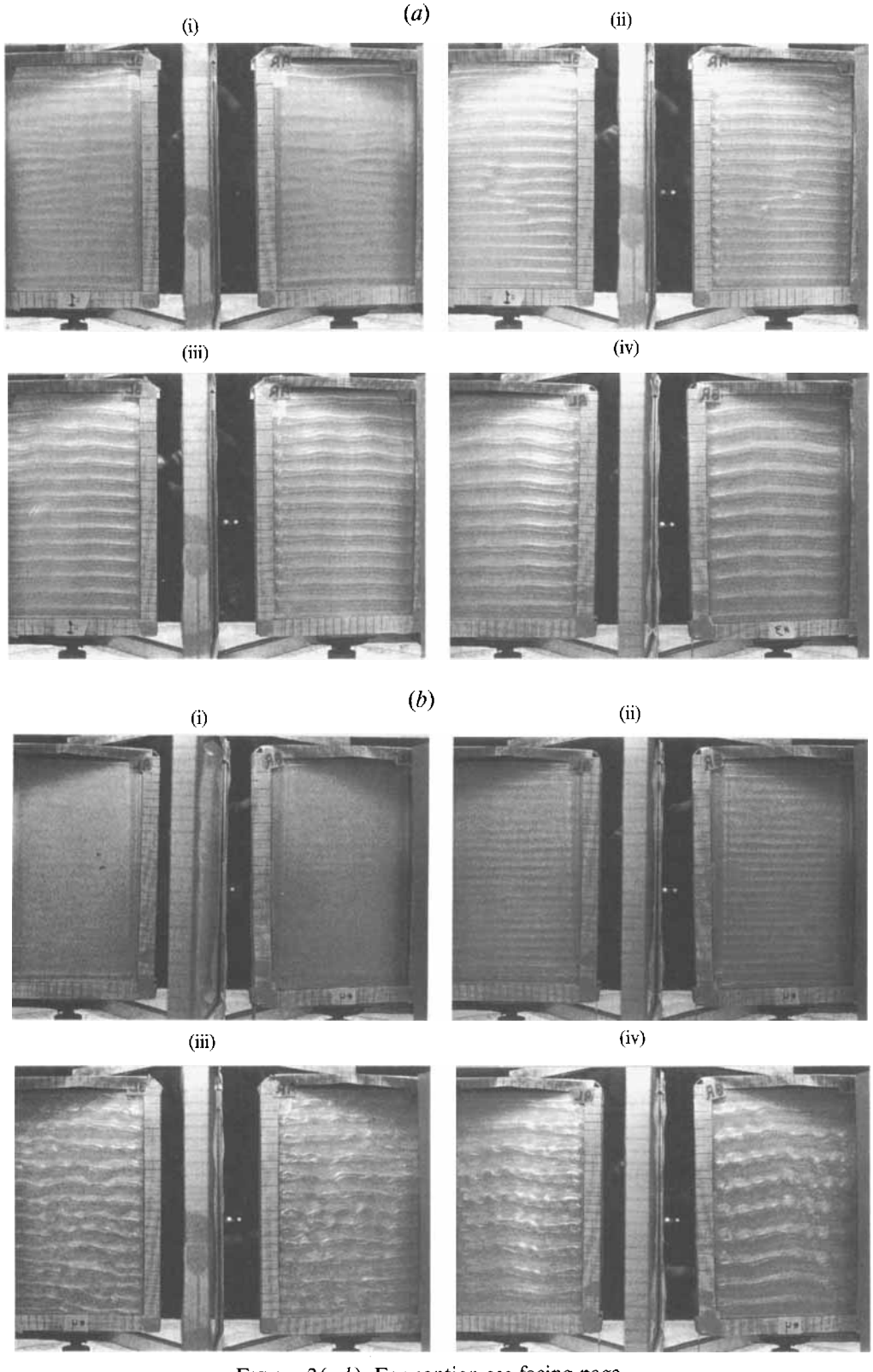

FIGURE 2(*a*,*b*). For caption see facing page.

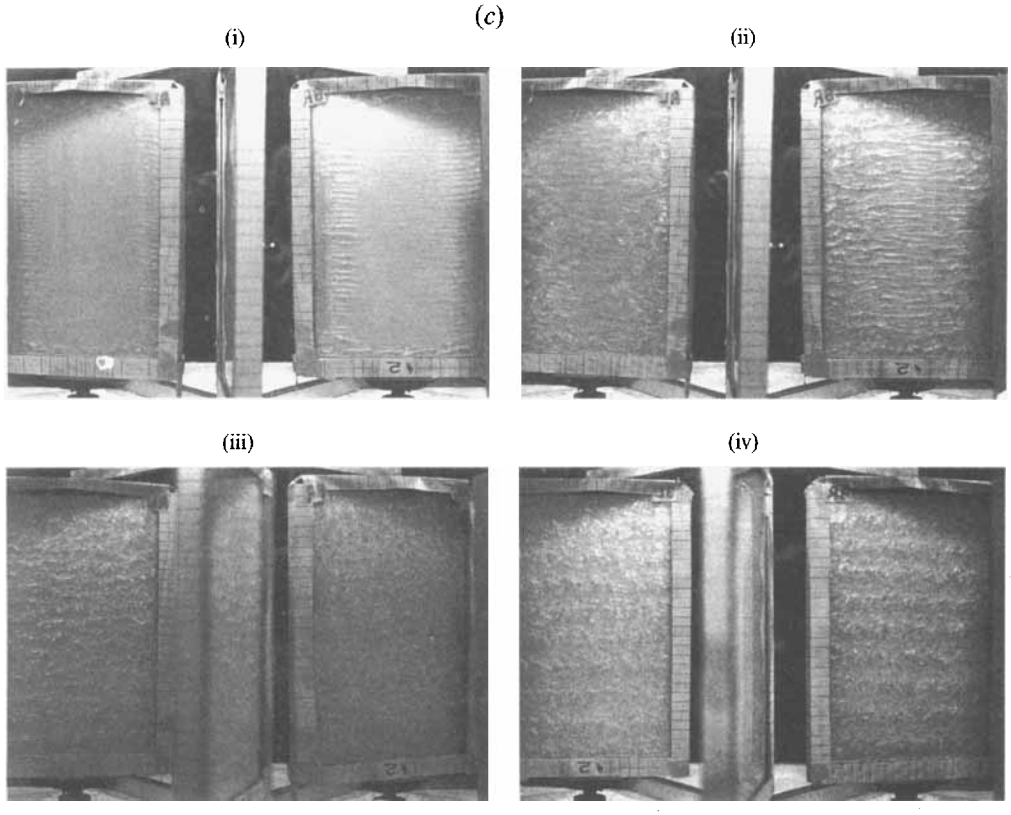

FIGURE 2. Photographs of evolution after an impulsive start ($d = 0.8$ cm, fluid: water with Kalliroscope visualization, cell 1, orientation $L_z = L$). Four views of the cell are shown with time increasing from (i) to (iv). Each part shows both sides of the cell, reversed as the view was in mirrors at right angles, with $\alpha = 90°$. At the moment the photographs were taken, the instantaneous angle, θ, was near an extremum, $\theta \approx \pm\alpha$. The notable trends are as follows: For larger Φ, the initial onset wavelength is smaller, but the final equilibrium wavelength is larger. The progression to an equilibrium state is more rapid for larger Φ. The number of cycles which had past after the impulsive start when the photograph was taken is denoted m. Wavelength evolution measured from these and other photographs in the sequence is shown in figure 5, which also identifies the observed states. Centimetre-scale graph paper is visible at the edges of the cell. (*a*) $\Phi = 72.6$: (i) $m = 4$, (ii) $m = 10$, (iii) $m = 192\frac{1}{2}$, (iv) $m = 334$. (*b*) $\Phi = 126.0$: (i) $m = 2$, (ii) $m = 4$, (iii) $m = 23\frac{1}{2}$, (iv) $m = 98$. (*c*) $\Phi = 400.7$: (i) $m = 4\frac{1}{2}$, (ii) $m = 6\frac{1}{2}$, (iii) $m = 8\frac{1}{2}$, (iv) $m = 104$.

3.1.1. *Onset of weak rolls*

For sufficiently small values of the frequency parameter Φ, or the angle α, no pattern could be observed in the dilute Kalliroscope solution. This is indicative of a pattern independent of z, and corresponds to the basic-state oscillatory shear flow (discussed further in §4). For somewhat higher values of Φ (or α), horizontal striations appeared, indicating the onset of weak irregular rolls (○). The symbols shown in parentheses are those which are used in figures 3–5. With greater forcing, the rolls increased somewhat in amplitude. This pattern of weak rolls was observed both with (○) and without (○) defects. The weak roll pattern is similar to what appears in part (i) of figure 2(*a–c*). When no defects were present, the roll pattern generally appeared uniform across the width of the cell, except near the lateral boundaries, lending support to the use of the near-axis approximation (also discussed in §4) for a stability analysis of the basic-state

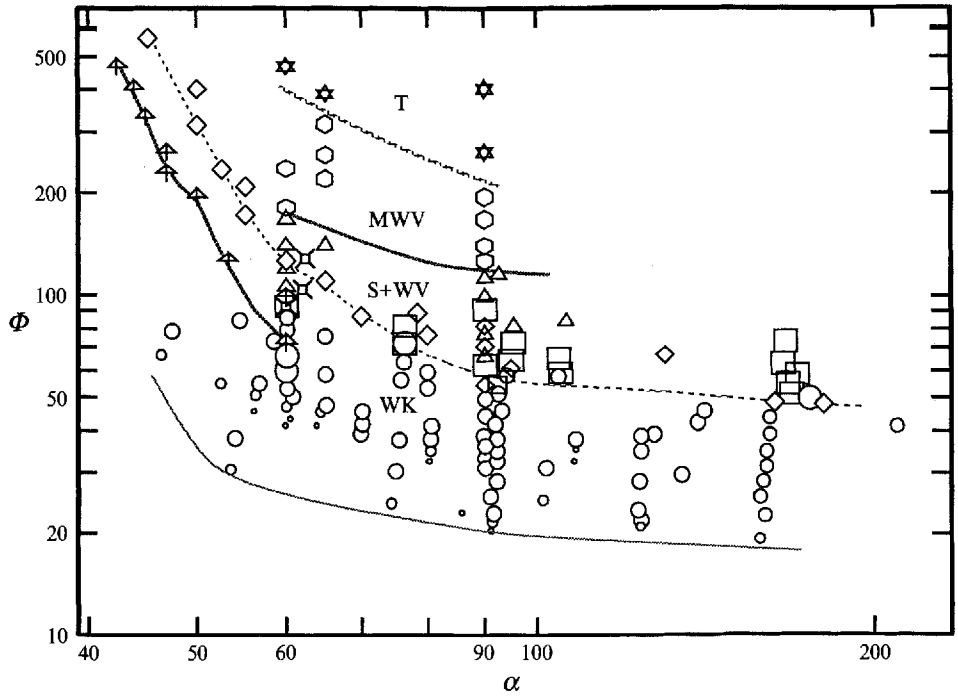

FIGURE 3. Φ–α regime diagram for weak and strong rolls: the non-dimensional frequency, $\Phi = \omega d^2/\nu$ versus the angle α (in degrees). The various symbols represent different flow states observed visually for five different cells (see table 1) and two different fluids (water and acetone). The grey curves show roughly where flow states are separated. Below the lower curve (and below some of the smallest circles), no structure could be observed in the cell, indicative of a nearly homogeneous basic-state shear flow. The symbols are as defined in §3.1. The weak roll state was observed in the region WK. Straight strong rolls (S) and strong rolls with laminar wavy modes (WV) occur with greater forcing. For larger Φ, we observed wavy modes of several wavelengths (MWV) and turbulence with coherent roll structure (T). The distinction between MWV and T states, near the upper curve, was not clear, whereas the distinction between MWV and WV was somewhat clearer. The middle curve separates WK from S upon increasing Φ. A curve also connects the data points where strong rolls disappeared upon a decrease of Φ(⟡, hysteresis).

shear profile. The wavelengths observed in the equilibrium state are displayed in figure 4, as discussed in §3.2.

3.1.2. *Strong rolls, wavy mode and transition to turbulence*

For greater forcing, an abrupt increase in the amplitude of the rolls was observed, often accompanied by a longer-wavelength state. The onset of strong rolls upon increase of Φ is indicated by (◇), whereas laminar strong rolls supercritical to onset is indicated by (□). It was clear that the strong rolls were associated with fluid motion through the fluid midplane ($y = 0$). Neighbouring rolls turned in opposite directions, so that the zero-frequency (temporal mean) component of fluid motion in the rolls ($\tilde{\boldsymbol{u}}_0$) possessed vorticity either in the positive or negative $\hat{\imath}$-direction ($\nabla \times \tilde{\boldsymbol{u}}_0 \parallel \pm\hat{\imath}$). Hall's (1994) linear stability analysis predicts well the onset of the strong-roll regime (curve $T1$ of his figure 3). At times the strong-roll state initiated from the top and/or bottom of the cell, and moved as a travelling front (⋈), consuming the weak-roll state, and then persisted throughout the entire cell. The existence of such a travelling front suggests that the onset of the strong rolls may be associated with a subcritical bifurcation.

Indeed, we did observe hysteresis of the strong-roll state for $\alpha \lesssim 90°$. We indicate the disappearance of the strong-roll state upon decrease of Φ by (⏃) in figure 3. As was the case for the weak rolls, the strong-roll state was observed both with and without defects. The pattern of strong rolls with defects is similar to that displayed in figure 2(*a*)(ii). When no defects were present, the rolls appeared to have a nearly constant amplitude across the width of the cell. Wavelength adjustments often took place by the creation and elimination of defects, as discussed further below.

For somewhat stronger forcing, the roll state lost its lateral homogeneity and gave rise to a wavy instability (△) (with wave vector in the x-direction). The pattern is similar to figure 2(*a*)(iii) and (iv). The locations in the Φ–α parameter space for which defects and wavy instabilities occurred must, of course, depend on the roll wavelength present. The wavelength present is itself influenced by the quantization of the rolls, due to finite boundaries in the z-direction. For even greater forcing, the once-laminar wavy rolls became more irregular, with several superimposed wavy modes (⬡) (cf. figure 2(*b*)(iv)). It appeared that a somewhat turbulent state could exist, superimposed on a wavy-roll state. The wavelength of the wavy instability generally decreased as Φ was increased. For the highest forcing, we observed a very turbulent state (✡), superimposed on a well-defined roll structure (cf. figure 2(*c*)(iv)). With the exception of the distinction between the weak- and strong-roll states, this series of transitions is reminiscent of the typical flow regimes observed in Taylor–Couette flow (see Coles 1965; Fenstermacher, Swinney & Gollub 1979; Koschmieder 1979). It also appears that there may be an onset of turbulence coincident with the onset of strong rolls for large Φ and small α (possibly around $\Phi = 700$ and $\alpha = 43$), although further experimental work is necessary to resolve this.

3.2. *Preferred equilibrium wavelengths*

The equilibrium wavelengths observed are presented in figure 4. After equilibrium was obtained, the oscillation was stopped and the rolls or roll pairs remnant in the Kalliroscope visualization were counted over a measured distance. There was at times an ambiguity concerning whether one was counting rolls or roll pairs for the weak-roll regime. This could introduce a factor of 2 error in some of the low-Φ, small-λ/d, weak-roll data points in figure 4 (some of the small wavelengths possibly should be doubled). In general, larger wavelengths were observed for larger values of Φ, with some overlap between adjacent regimes. A similar tendency for increase in wavelength with stronger forcing has also been observed in a number of flow regimes, including Taylor–Couette flow and Rayleigh–Bénard convection. The wavelengths for onset of the strong rolls appear to be well captured by Hall's (1994) linear stability analysis (cf. curve $T1$ of his figure 4).

We also observed hysteresis in the equilibrium wavelengths, especially in the straight, strong-roll and wavy regimes. Upon a gradual increase in Φ, with α fixed, the wavelengths tended to increase (by creation and elimination of defects) along a particular path in (λ/d)–Φ space. Upon gradual decrease in Φ, the wavelengths would decrease, but would maintain a higher wavelength than the path followed during an increase of Φ. It would be possible to establish the stability boundaries separating straight-laminar strong rolls and wavy rolls by examination of such behaviour.

3.3. *Front propagation*

Travelling fronts of strong rolls consuming weak rolls were observed in several regions of the Φ–α parameter space. This was typical for large increases of the driving frequency, and impulsive starts, but was also observed upon extremely small increases

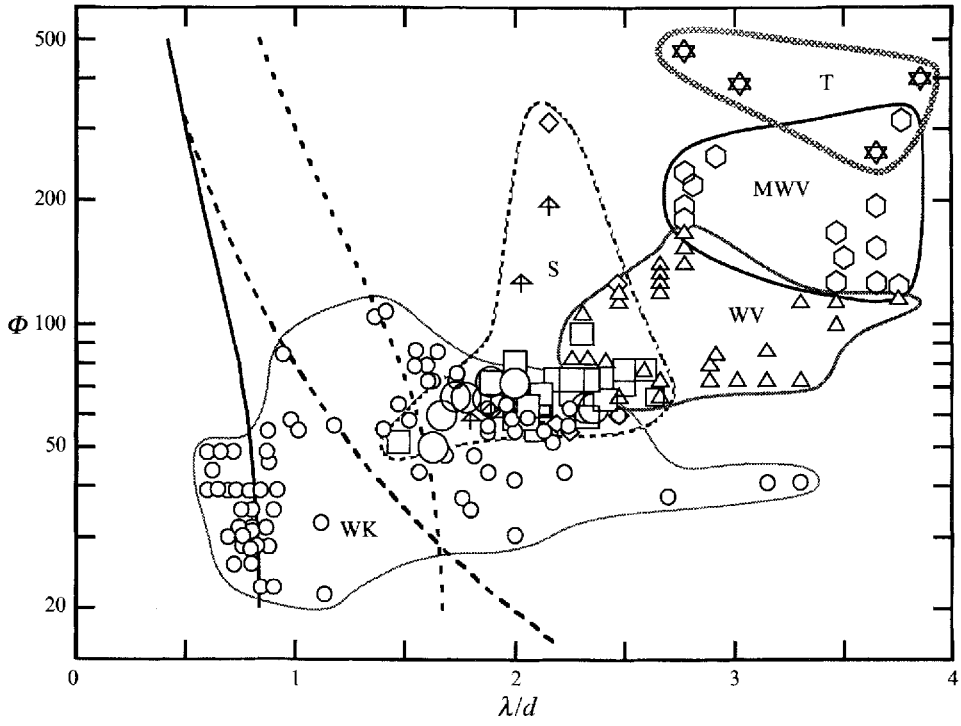

FIGURE 4. Final equilibrium wavelengths: the wavelengths non-dimensionalized by the gap spacing are shown for various values of the frequency parameter $\Phi = \omega d^2/\nu$. This figure contains results for all investigated values of the angle α. The symbols and letters indicating the observed regimes are defined in §3.1 and figure 3. Note that the general tendency shows larger equilibrium non-dimensional wavelengths for larger forcing, while there is some overlap between each regime. The curved enclosures serve only to separate the observed regimes. The $\lambda/d \geqslant 3$ of the weak-roll state near $\Phi = 40$ were for large $\alpha(\alpha = 217°)$. The long-dashed line is $2\pi\delta_S/d$, where δ_S is the Stokes-layer thickness (note that $\delta_S/d = (2/\Phi)^{\frac{1}{2}}$). We include this curve for reference; but it is not as relevant as the solid curve $(4\xi/d)$ or the short-dashed curve $(8\xi/d)$, especially for small Φ. These scalings for λ/d at onset are discussed further in §4.4. In §3.2, we note a possible factor of 2 ambiguity in the low-Φ, small-wavelength data points for the weak-roll regime. The proper resolution of this ambiguity may shift some of the clustering about the $4\xi/d$ curve to about the $8\xi/d$ curve.

in Φ, transcending the strong-roll onset. This indicates that the strong-roll onset may contain regions governed by a subcritical instability. For purposes of comparison to future studies, we report that the speed of the propagating strong-roll front was $0.0875\ \mathrm{cm}^{-1}\ \mathrm{s}$ for $\Phi = 92.4$, $\alpha = 60°$ (cell 1, orientation: $L_z = L$, fluid: water). Hysteresis was not detectable for $\alpha \gtrsim 90°$.

3.4. *Structure and wavelength evolution after an impulsive start*

Photographs were taken at various moments following an impulsive start from a rest state (figure 2). End effects are apparent in this photo-sequence. For low Φ, a strong roll was sometimes present at the top, and another at the bottom. This feature was often observed both in the weak-roll equilibrium state and during the transient weak-roll state after an impulsive start. Part (i) of each of figures 2(*a*)–2(*c*) shows a stronger roll at the top and bottom soon after an impulsive start. Also, lateral inhomogeneity is quite apparent in the high-Φ sequence (figure 2(*c*)(i) and (ii)), where the rolls grew somewhat more quickly near the lateral edges than in the centre. We note, however,

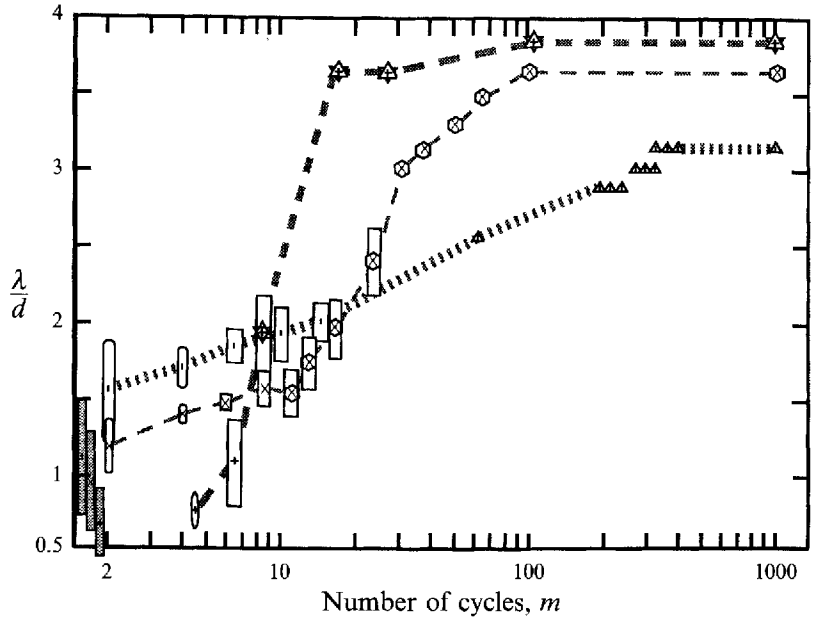

FIGURE 5. Wavelength evolution after an impulsive start: the wavelength, non-dimensionalized by the gap spacing d, is shown as a function of m, the number of cycles after an impulsive start. The interior symbols |, ×, and +, correspond to $\Phi = 72.6$, 126.0 and 400.7, respectively. All of these cases are for $\alpha = 90°$. Several photographs of the sequence from which these wavelengths were measured are shown in figure 2. For low m, the boxes with rounded ends correspond to the flow pattern characteristic of weak rolls. By $m = 7$, all cases shown here exhibited strong-roll characteristics. The other symbols are as defined in §3.1. The range of wavelengths observed is indicated by the vertical extent of the box. The grey lines serve only to connect points of observation. For the laminar wavy state, wavelength adjustment took place by discrete jumps, through the creation and elimination of defects, as is apparent for $\Phi = 72.6$ with m between 200 and 300. The small shaded rectangles near the left axis indicate the range between $4\xi/d$ and $8\xi/d$ for each of the runs (cf. §4.4). (See figure 2 caption for cell number and orientation.)

that the final equilibrium state for all three cases exhibits a laterally homogeneous pattern, except for the presence of wavy instabilities or turbulent motion superimposed upon the persistent roll state.

The wavelength evolution after an impulsive start is shown in figure 5. These wavelengths were measured (along typically 4 or 5 equally spaced vertical lines) from a series of photographs, some of which are presented in figure 2. Special care was taken to correct for the linear trends arising from mirror tilt and cell phase (not all photographs were taken precisely at $\theta = \pm\alpha$). There was certainly a larger distribution of wavelengths present in each photograph than could be measured by this technique. A two-dimensional Fourier analysis would show this, but it would also contain features peculiar to the Kalliroscope visualization. We have not investigated the possible influence which a variable aspect ratio may have on the rates of wavelength adjustment.

The initial wavelength selected is small when the driving frequency is large, in accordance with the small Stokes-layer thickness for large Φ (although a more relevant measure is, ξ, the distance between the wall and the location of $\bar{U}_{max}$: see §4.1), but the final wavelength is large for large Φ. The high-wavelength, coherent-roll structure of the turbulent state has also been observed in Taylor–Couette experiments.

In the laminar-wavy regime, wavelength adjustment took place by the creation and

elimination of defects. For a constant forcing frequency, wavelengths would not decrease (although they could decrease upon a decrease of Φ). What we now describe was observed during an increase of wavelength. The amplitude of the wavy instability appeared to grow slowly in amplitude, until a defect was nucleated near the cell edge (say near $x = +\frac{1}{2}L_x$). Soon afterwards, another defect would appear on the other cell edge (near $x = -\frac{1}{2}L_x$) on the same roll pair. A series of defect glides would occur so as to propagate the defects toward the upper (or lower) cell boundary. The roll wavelengths throughout the cell gradually relaxed to a larger value as a roll would be eliminated at the top (or bottom) of the cell.

4. Basic-state shear in the near-axis approximation

In this section we address the oscillatory basic-state shear flow before the onset of rolls.

4.1. *Analytical form of the velocity profile*

The equations governing the flow of an incompressible fluid in the oscillatory rotating frame are

$$\left.\begin{aligned} \frac{\partial \boldsymbol{u}}{\partial t} + \boldsymbol{u}\cdot\nabla\boldsymbol{u} + 2\boldsymbol{\Omega}\times\boldsymbol{u} + \frac{\nabla p}{\rho} - \nu\nabla^2\boldsymbol{u} + \boldsymbol{\Omega}\times(\boldsymbol{\Omega}\times\boldsymbol{r}) + \dot{\boldsymbol{\Omega}}\times\boldsymbol{r} = \boldsymbol{0}, \\ \nabla\cdot\boldsymbol{u} = 0, \end{aligned}\right\} \tag{1}$$

where $\boldsymbol{u}$ is the fluid velocity. The position vector from the origin is $\boldsymbol{r}$, ρ is the fluid density, ν is the kinematic viscosity, p is pressure, $\Omega(t)$ is the time-dependent angular velocity ($\boldsymbol{\Omega} = \Omega\hat{\boldsymbol{k}}$, and $\dot{\boldsymbol{\Omega}} = (\partial\boldsymbol{\Omega}/\partial t)$). The $\dot{\boldsymbol{\Omega}}\times\boldsymbol{r}$ term in the momentum equation has been called the 'Euler force' by Lanczos (1970). In what follows, refer to the coordinate system as defined in §2.1. For pure harmonic forcing, we may choose the instantaneous angle of the cell from its mean position in the fixed laboratory frame as $\theta = -\alpha\cos(\omega t)$, which implies that $\Omega = \alpha\omega\sin(\omega t)$ (cf. figure 1*a*). The balance of gravitational forcing with a hydrostatic pressure distribution, for constant-density fluids, has been already removed from (1).

The basic-state shear velocity in a finite box is a function of all three spatial directions and time. In a cell with infinite vertical extent, but finite boundaries in the x- and y-directions, it would depend only upon x, y and t. As the gap spacing, d, is much smaller than the width of the cell, L_x, the flow near the centrally located rotational axis is primarily in the $\pm x$-direction, with $|\partial u/\partial y| \gg |\partial u/\partial x|$. This suggests a model for the basic-state shear velocity near the axis in which we write

$$\boldsymbol{u} = \hat{\boldsymbol{\imath}}\bar{U}(y,t).$$

Visual observations of particle advection in the basic-state shear support this assumption, as does the nearly x-independent structure of the rolls after their onset. In what follows, we refer to the simplified form of the velocity profile with $\partial\boldsymbol{u}/\partial x = 0$ as satisfying the 'near-axis approximation'.

We seek a solution for the basic-state flow of the form $\boldsymbol{u} = \hat{\boldsymbol{\imath}}\bar{U}(y,t)$. We make this substitution, and operate on the momentum equation (1) by $\hat{\boldsymbol{k}}\cdot\nabla\times$ to yield

$$\bar{U}_{yt} = \nu\bar{U}_{yyy} + 2\Omega_t, \tag{2}$$

where subscripts represent partial derivatives. Rigid boundary conditions are imposed at $y = \pm b$, where $b = \frac{1}{2}d$. We substitute

$$\bar{U} = \bar{V}(y)\exp(\mathrm{i}\omega t) + \bar{V}^*(y)\exp(-\mathrm{i}\omega t)$$

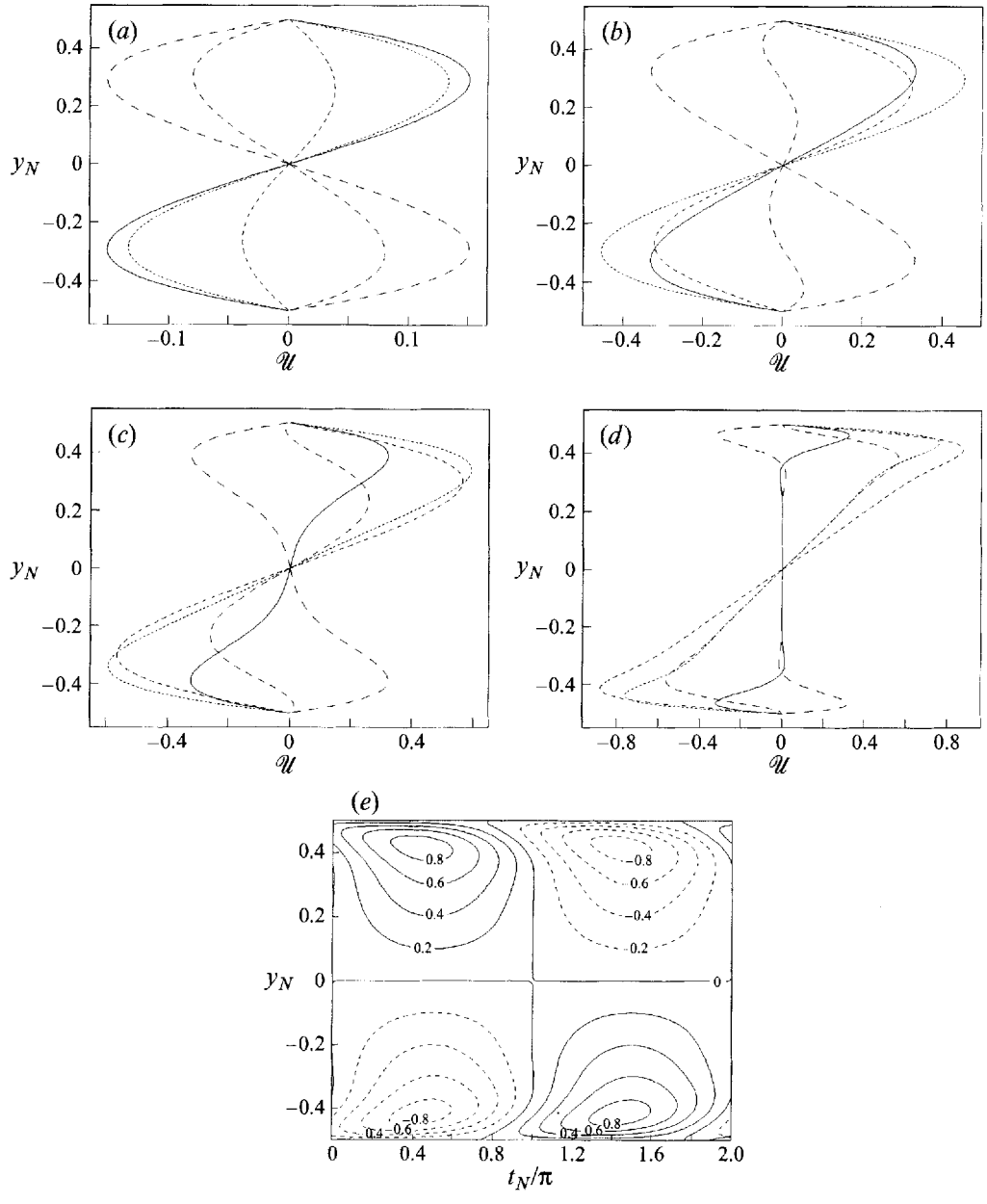

FIGURE 6. Analytical solutions for the basic-state shear velocity in the $\hat{\imath}$ direction, for various values of the non-dimensional frequency parameter Φ, in the 'near-axis approximation' of §4.1, in the oscillatory reference frame. In (*a–d*), the abscissa is the modified velocity $\mathscr{U}$ ($\mathscr{U} = \bar{U}/\alpha\omega d$, with $\bar{U}$ from (3)). The ordinate is the cross-gap position $y_N = y/d$. Each part shows the velocity profiles for five different phases of the flow, starting with the solid line, and progressing to lines with longer dashes. We have chosen the phase such that $\Omega = \alpha\omega\sin(\omega t)$; and the five phases correspond to $\omega t = n\pi/4$, with $n = 0$ to 4. The phases $n = 5$ to 7 (not shown) are mirror symmetric about $\mathscr{U} = 0$ to phases 1 to 3. In all cases, there is an inflexion point at $y = 0$. Additional inflexion points may occur at other locations and are phase dependent. (*a*) $\Phi = 10$, (*b*) $\Phi = 40$, (*c*) $\Phi = 100$, (*d*) $\Phi = 1000$. (*e*) Contours of the modified velocity $\mathscr{U}$, for $\Phi = 1000$. The abscissa is the non-dimensional time (ωt) divided by π.

into (2), where the asterisk denotes the complex conjugate. We find that

$$\bar{V}(y) = -\mathrm{i}\alpha\omega b\left(\frac{y}{b} - \frac{\sinh(gy)}{\sinh(gb)}\right),$$

where $g = (\mathrm{i}\omega/\nu)^{\frac{1}{2}}$. In terms of real quantities, the solution is

$$\begin{aligned}\bar{U}(y,t) = 2\alpha\omega y\sin(\omega t) + \frac{2\alpha\omega b}{\cosh(2\gamma)-\cos(2\gamma)} \\ \times\{\cosh(\gamma)\sin(\gamma)(-\mathrm{e}^{-\beta y}\cos(\beta y-\omega t)+\mathrm{e}^{\beta y}\cos(\beta y+\omega t)) \\ +\sinh(\gamma)\cos(\gamma)(-\mathrm{e}^{-\beta y}\sin(\beta y-\omega t)-\mathrm{e}^{\beta y}\sin(\beta y+\omega t))\}. \end{aligned} \tag{3}$$

Here, $\beta = (\omega/(2\nu))^{\frac{1}{2}}$ and $\gamma = b\beta$. Note that the factor β is the inverse of the oscillatory Stokes-layer thickness ($\delta_S = (2\nu/\omega)^{\frac{1}{2}}$) and that γ is related to the frequency parameter Φ by $8\gamma^2 = \Phi$.

The solution for the basic-state velocity profile in the near-axis approximation contains a wealth of information. It may be used to define a Reynolds number and to serve as a basic state for an analysis of stability. The velocity used in the definition of a Reynolds number for this oscillatory problem could be $\bar{U}_{max}$, the maximum absolute value of $\bar{U}$ over all phases and all relevant values of y. Also of relevance is ξ, the distance between the wall and the location of $\bar{U}_{max}$ (i.e. $\xi = d(\frac{1}{2} - y_m)$, where y_m is the non-dimensional y-location of the maximizing velocity). We shall use the gap spacing d as a lengthscale and ω^{-1} as a timescale. Here we define a modified velocity $\mathscr{U} = \bar{U}/(\alpha\omega d)$, which is the non-dimensional velocity divided by the angle α. In this form, the modified velocity $\mathscr{U}$ only depends upon Φ and the non-dimensional time and distance, $t_N = \omega t$ and $y_N = y/d$. Note that $\mathscr{U}$ is independent of α. (This $\mathscr{U}$ is identical to $\bar{u}$ of Hall (1994, equation (2.8)).) Figure 6 shows the y_N dependence of $\mathscr{U}$ for various values of the phase t_N. We define $Re^d = \bar{U}_{max}\, d/\nu$, so that $Re^d = \alpha\Phi\mathscr{U}_{max}$. In figure 7, we show how $\mathscr{U}_{max}$ depends upon Φ, as well as the values of the non-dimensional time and distance for which the maximum velocity is achieved (t_m and y_m – calculated from (3) using a parabolic fitting routine in both t_N and y_N). By symmetry, we may restrict our attention to $0 \leqslant y_N < \frac{1}{2}$ and $0 \leqslant t_N < \pi$. Similar maximal absolute values will occur for negative values of y_N and phase shifts of π.

The average kinetic energy per unit mass for the basic-state shear in the oscillating frame is

$$\bar{K} = \frac{1}{2}\frac{1}{V\tau}\int_0^\tau \mathrm{d}t\int_V \mathrm{d}V(\bar{U}\cdot\bar{U}).$$

Here, τ is the period of cell oscillation and V is a volume of integration. We may use the x- and z-independence of the basic state, and the non-dimensionalization described above, to find that $\bar{K} = (\alpha\omega d)^2\bar{\mathscr{K}}/4\pi$, where

$$\bar{\mathscr{K}} = \int_0^{2\pi}\mathrm{d}t_N\int_{-\frac{1}{2}}^{\frac{1}{2}}\mathrm{d}y_N(\mathscr{U}^2). \tag{4}$$

If we scale the velocity by $\bar{U}_{max}$, we may write $\bar{K} = \frac{1}{2}\bar{P}\bar{U}_{max}^2$. The form factor $\bar{P}$ depends upon the time-dependent structure of the velocity field, and it ranges between 0.16 (for low Φ) and 0.26 (for high Φ). In figure 7, we also show the dependence of $\bar{\mathscr{K}}$ upon Φ. If we had scaled the velocity by the root-mean-square velocity, v_{rms}, the form factor would be 1, but v_{rms} would still be dependent on Φ.

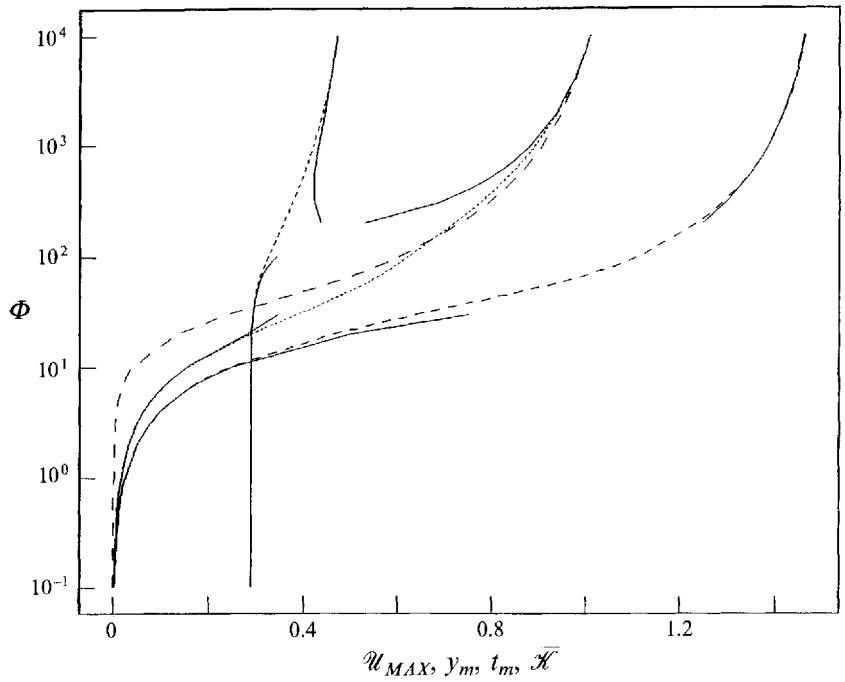

FIGURE 7. The Φ dependence of $\mathscr{U}_{max}$, y_m, t_m and $\bar{\mathscr{K}}$: $\mathscr{U}_{max}$ is the maximum of the modified velocity ($\mathscr{U} = \bar{U}/(\alpha\omega d)$) over the phases $0 \leqslant t_N = \omega t < \pi$ and over locations $0 \leqslant y_N = y/d < \frac{1}{2}$. The phase of t_N for which the velocity achieves its maximum is t_m, and y_m is the corresponding location of y_N. The non-dimensional kinetic energy, $\bar{\mathscr{K}}$, is as defined in equation (4). The dashed curves are, respectively with longer dashes, $\mathscr{U}_{max}$, y_m, t_m and $\bar{\mathscr{K}}$. These were calculated numerically using the velocity solution given in (3). The truncated solid curves are the low- and high-frequency limits, from (6) and (8).

4.2. *Low-frequency limit*

The limits of high and low dimensionless frequencies provide simplified forms for $\mathscr{U}$. These forms will be useful for comparison to future experiments which span a wider range of parameter space, and for asymptotic stability theories. For low frequencies, after expanding for small γ (recall that $8\gamma^2 = \Phi$), we find that

$$\mathscr{U}^{low} = \gamma^2(\tfrac{2}{3}y - \tfrac{8}{3}y^3)\cos(t) + \gamma^4(\tfrac{7}{45}y - \tfrac{8}{9}y^3 + \tfrac{16}{15}y^5)\sin(t) + \gamma^6(-\tfrac{31}{945}y + \tfrac{28}{135}y^3 - \tfrac{16}{45}y^5 + \tfrac{64}{315}y^7)\cos(t), \quad (5)$$

where we have dropped the subscripts, but both t and y are to be understood as the non-dimensional quantities t_N and y_N. (The lowest-order terms correspond to Hall (1994, equation (2.11)).) We also find that

$$t_m = t_2\gamma^2, \quad y_m = y_0 + y_4\gamma^4, \quad (6a, b)$$

$$\mathscr{U}^{low}_{max} = \frac{2}{9(3)^{\frac{1}{2}}}\gamma^2 - \frac{191}{42\,525(3)^{\frac{1}{2}}}\gamma^6, \quad (6c)$$

where t_m and y_m represent the phase and non-dimensional cross-gap location for which the maximum velocity $\mathscr{U}^{low}_{max}$ is achieved in the interval $0 \leqslant y < \frac{1}{2}$ and $0 \leqslant t < \pi$. In §§4.2 and 4.3, all times and locations are non-dimensional. Here, y_0 and y_4 were determined from the condition that $\partial\mathscr{U}/\partial y = 0$ at orders γ^2 and γ^6, respectively; and t_2 was found from the condition that $\partial\mathscr{U}/\partial t = 0$ at order γ^4 ($y_0 = 1/(12)^{\frac{1}{2}}$, $y_4 = 17(3)^{\frac{1}{2}}/85050$, and $t_2 = \frac{1}{5}$). For $\Phi \to 0$, we have $\xi \to d(\frac{1}{2} - 1/(12)^{\frac{1}{2}})$. Figure 7 shows

how the actual t_m and y_m correspond to values calculated from the frequency limits. The low-frequency limit used by Hall (1994) diverges from the actual values more rapidly than the low-frequency limit shown in figure 7.

4.3. *High-frequency limit*

For high frequencies, again dropping the N subscripts, we find that

$$\mathscr{U}^{high} = 2y\sin(t) - e^{\gamma(2y-1)}\sin(\gamma(2y-1)+t) = (1-\epsilon)\sin(t) + e^{-\epsilon\gamma}\sin(\epsilon\gamma - t), \quad (7)$$

where $\epsilon = 1-2y$. (This $\mathscr{U}^{high}$ is equivalent to Hall (1994, equation (2.10)).) In order to find the modified velocity maximum, over all phases and positions, we must satisfy $\partial\mathscr{U}/\partial\epsilon = 0$ and $\partial\mathscr{U}/\partial t = 0$ simultaneously. We again let t_m and ϵ_m represent the phase and location which satisfy the above conditions for an extremal velocity, as in §4.2. For large γ the limiting forms of t_m and ϵ_m are

$$t_m = t_0 + \frac{t_1}{\gamma}, \quad \epsilon_m = \frac{\epsilon_1}{\gamma} + \frac{\epsilon_2}{\gamma^2}, \quad (8a, b)$$

where t_0, t_1, ϵ_1, and ϵ_2 are constants to be determined. We obtain

$$\begin{aligned}
&\epsilon_1 - t_0 = \tfrac{1}{4}\pi, && \text{from } \partial\mathscr{U}/\partial\epsilon = 0 \text{ at } O(\gamma);\\
&\cos(\epsilon_1 - \tfrac{1}{4}\pi) - \tfrac{1}{2}(2)^{\frac{1}{2}}e^{-\epsilon_1} = 0, && \text{from } \partial\mathscr{U}/\partial t = 0 \text{ at } O(1);\\
&t_1 = \frac{\sin(t_0) + \epsilon_1\cos(t_0)}{\tfrac{1}{2}(2)^{\frac{1}{2}}e^{-\epsilon_1} - \sin(t_0)}, && \text{from } \partial\mathscr{U}/\partial\epsilon = 0 \text{ at } O(1);\\
&\epsilon_2 = t_1 - \tfrac{1}{2}(2)^{\frac{1}{2}}(e^{\epsilon_1}\sin(t_0)), && \text{from } \partial\mathscr{U}/\partial t = 0 \text{ at } O(1/\gamma).
\end{aligned}$$

The $O(1)$ condition from $\partial\mathscr{U}/\partial t = 0$ may be solved for ϵ_1 by Newton–Raphson iteration ($\epsilon_1 = 2.284\,102\,297\,39\ldots$), while the other constants may be evaluated algebraically. The value of $\mathscr{U}^{high}_{max}$ is obtained by evaluating $\mathscr{U}^{high}$ at t_m and ϵ_m, i.e.

$$\mathscr{U}^{high}_{max} = (1-\epsilon_m)\sin(t_m) + e^{-\epsilon_m\gamma}\sin(\epsilon_m\gamma - t_m). \quad (8c)$$

Both the high- and low-frequency limits are displayed in figure 7. Note that the Stokes-layer thickness, $\delta_S = (2\nu/\omega)^{\frac{1}{2}}$, does not correspond to the distance ξ. In the high-frequency limit, to order $1/\gamma$, we have $\xi = 4\epsilon_1\delta_S$.

4.4. *Simple resonance conditions*

For moderate to high Φ, the strong-roll state may be associated with resonance. This was suggested by an apparent synchronicity of the roll turnover time with the period of the forcing (observed visually). A simple scaling analysis will yield conditions for resonance. Our primary requirement is that sufficient kinetic energy should be available in the basic state from which a resonant roll may be driven. Resonance occurs when the roll turnover time equals the period of cell oscillation. For a resonant roll to exist, the kinetic energy associated with the roll cannot exceed the kinetic energy of the basic state. For this we write $\bar{K} \geqslant A_0\tilde{K}_0$, where $\bar{K}$ is defined in §4.1, and A_0 is a constant of $O(1)$. Formally, we define $\tilde{K}_0$ to be the average kinetic energy per unit mass of the zero-frequency component of the roll velocity (we retain the near-axis approximation and use $\boldsymbol{u} = \bar{\boldsymbol{U}} + \tilde{\boldsymbol{u}}$, where $\tilde{\boldsymbol{u}}$ contains both the time-periodic and zero-frequency components of the perturbation roll velocity). The zero-frequency component of the roll velocity is

$$\tilde{\boldsymbol{u}}_0(y,z) = \frac{1}{\tau}\int_0^\tau \mathrm{d}t\,(\boldsymbol{u}(y,z,t)),$$

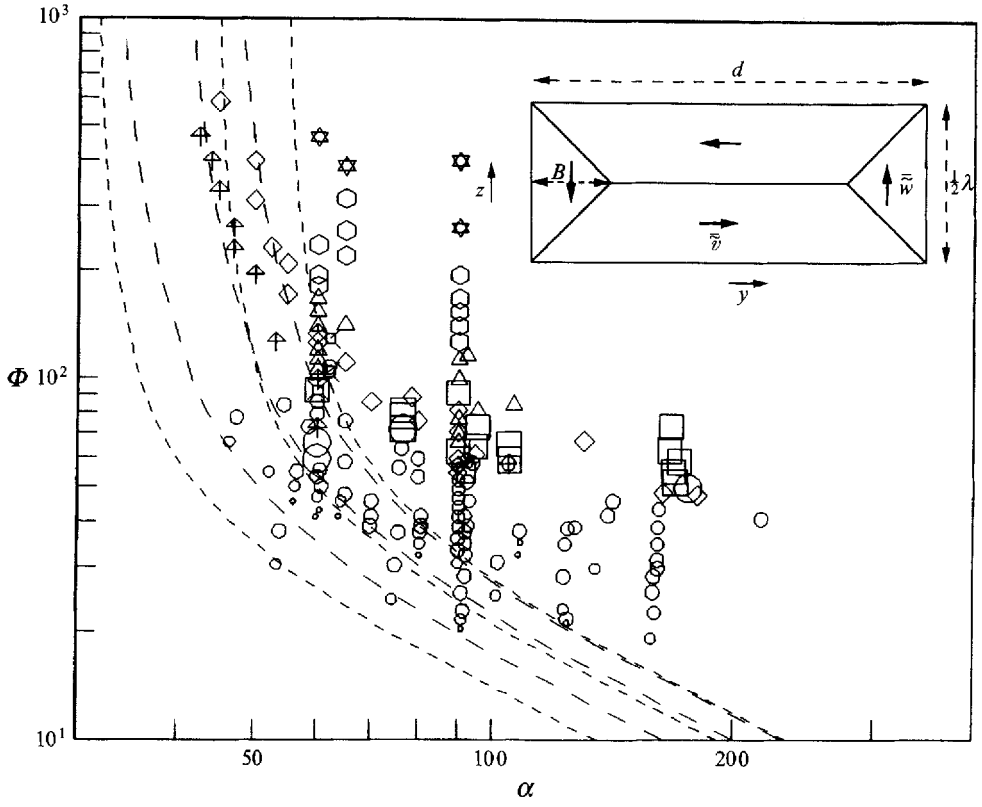

FIGURE 8. Resonance conditions with data: the data of figure 3 are displayed with the resonance conditions of §4.4 (equations (9)), for various values of A_0 (larger A_0 yield curves with larger α). The inset shows the (y, z) cross-section of a roll. The short-dashed curves are from the [RS] model for rectangular strong rolls, with $A_0 = 0.5$, 1.0 and 1.5. The curves with long dashes are from the [SS] model for square-section strong rolls, with $A_0 = 0.5$, 0.75 and 1.0.

where τ is the period of the forcing, $\tau = 2\pi/\omega$. We define

$$\tilde{K}_0 = \frac{1}{2}\frac{1}{A}\int \mathrm{d}A\,(\tilde{\boldsymbol{u}}_0 \cdot \tilde{\boldsymbol{u}}_0).$$

A full nonlinear simulation with rolls would be required to give the actual velocity field. In general we may write $\tilde{K}_0 = \frac{1}{2}\tilde{P}_0\bar{\tilde{v}}^2$, where $\tilde{P}_0$ is a form factor dependent upon the actual velocity structure, and $\bar{\tilde{v}}$ is a chosen velocity scale for the roll velocity in the y-direction. We have calculated $\tilde{P}_0$ for a variety of velocity structures; it ranges between 0.4 and 1. This form factor is larger than that of the basic state, partly due to the lack of time dependence in $\tilde{\boldsymbol{u}}_0$. In lieu of the actual velocities, we adopt the simplest velocity field which conserves mass and captures the structure of a roll. First to be considered is the structure shown inset in figure 8. The distance from a lateral edge to the nearest triangle vertex is B, and the vertical extent is half a wavelength ($\frac{1}{2}\lambda$). In each section of such a roll, we assign a magnitude of average velocity components, with the y- and z-components of the velocity being $\bar{\tilde{v}}$ and $\bar{\tilde{w}}$. To conserve mass we must have $\bar{\tilde{w}} = \lambda\bar{\tilde{v}}/(4B)$. With this crude approximation, we calculate $\tilde{K}_0$ for the rectangular strong-roll [RS] shape inset in figure 8. This somewhat overestimates $\tilde{P}_0$ (and $\tilde{K}_0$) compared to what the correct (unknown) velocity field would yield. We first suppose that the wavelength scales with the distance between the cell edge ($y = b$) and the y-

location for the maximum velocity ($y_m d$) in the form $\lambda = 4\xi$ (recall that $\xi/d = \frac{1}{2} - y_m$). For this scaling, we also choose $B = 2\xi$, which has the effect of making the centre of the region of vertical motion coincident with the region of maximum velocity of the basic state. The [RS] model then yields $\tilde{K}_0^{RS} = \frac{1}{2}\bar{\tilde{v}}^2 (1 - 3\xi/2d)$ and $\bar{\tilde{\tau}}^{RS} = 2d/\bar{\tilde{v}}$, where $\bar{\tilde{\tau}}$ represents an average turnover time for the roll. For resonance, we would have $\bar{\tilde{\tau}} = \tau$, τ being the period of cell oscillation. We use $\bar{K} = (\alpha\omega d)^2 \bar{\mathscr{K}}/4\pi$, from §4.1 just above equation (4), and the condition $\bar{K} \geqslant A_0 \tilde{K}_0$, to yield a resonance condition for rectangular strong rolls of the form

$$\bar{\mathscr{K}}\alpha^2 \geqslant \frac{2A_0}{\pi}\left(1 - \frac{3\xi}{2d}\right) \quad \text{[RS]}. \tag{9a}$$

The equality of this condition is shown in figure 8 for several values of A_0, along with another criterion developed below. For $\Phi \gtrsim 100$, the onset of strong rolls occurs near $A_0 = 1$. For lower Φ, where viscous effects would be more important, this criterion diverges rapidly from the experimental onset of strong rolls. Whether such resonance actually exists cannot be known until further experimental or numerical studies are completed.

Strong-roll resonance with square [SS] cross-section ($\lambda = 2d$) may be modelled using $B = \frac{1}{2}d$. After evaluating as described above, we find that $\tilde{K}_0^{SS} = \frac{1}{2}\bar{\tilde{v}}^2$, with $\bar{\tilde{\tau}}^{SS} = 2d/\bar{\tilde{v}}$, and

$$\bar{\mathscr{K}}\alpha^2 \geqslant \frac{2A_0}{\pi} \quad \text{[SS]}. \tag{9b}$$

Again, figure 8 shows that $A_0 = 1$ is in rough agreement with the experimental strong-onset data for $\Phi \gtrsim 100$. These strong-roll resonance models predict a small angle cut-off, i.e. an angle α below which no resonate rolls may be observed. (A longer wavelength rectangular [LRS] model with $\lambda = 8\xi$ and $B = 2\xi$ leads to the same resonance condition as [SS] above.) The $\lambda = 4\xi$ and $\lambda = 8\xi$ curves are included along with the wavelength data in figure 4. We emphasize that full nonlinear simulations are necessary in order to fully understand the onset and growth of the observed rolls.

5. Discussion

5.1. *Weak versus strong rolls*

The presence of weak rolls as the initial bifurcation from the oscillatory basic-state shear flow, and the subsequent bifurcation to a strong-roll state upon further increase of Φ, remains difficult to explain. Quantitative measurements of fluid velocities in the rolls would help shed light on this issue. However, such measurements may be difficult to obtain, given the oscillation of the cell. An analysis of stability of the basic-state oscillatory shear flow may also help distinguish different preferred states, although, given the apparent subcriticality of the strong-roll bifurcation for $\alpha \lesssim 90°$, a linear stability analysis may fail to resolve this issue. A full numerical solution for the nonlinear problem would be revealing, but is a formidable undertaking. Hall (1994) has addressed the linear stability in an asymptotic analysis. He maintains that the weak onset is associated with end effects.

Possibly, the weak rolls exist due to the higher harmonics introduced by the mechanical linkage. The plausibility of this is supported by the fact that the weak-roll onset occurs at a value of Φ roughly half of that for strong-roll onset. There is also the possibility that the weak rolls are just the lower-amplitude branch of an imperfect bifurcation with a subcritical bifurcation to the strong-roll state (cf. bottom of figure

III.9 of Iooss & Joseph 1980). Visual and photographic observations of the strong-roll state make it clear that the strong rolls have fluid motion through the fluid midplane ($y = 0$). Although weak rolls with small α do not penetrate through $y = 0$, we do not know if this also holds for the weak rolls at large α. It may be that the strong- and weak-roll differences may be due to differing structures.

5.2. *Relationships with other studies*

We have found no other studies which discuss the roll development in the oscillating cell; however, Hall (1994) has recently performed a linear stability analysis which appears to capture the strong-roll onset. The basic-state shear is oscillatory in nature with zero mean flow. We chose an oscillatory reference frame for the derivation of the velocity profile, because of the simplicity of the boundary conditions. In this frame, the maximum velocities occur in the fluid interior. An analysis in the fixed, laboratory frame would yield maximum velocities at the boundaries ($y = \pm\frac{1}{2}d$), as is the case for oscillatory Stokes layers.

As the basic-state shear is simply linear in α, both instantaneous and time-averaged inviscid stability criteria would yield neutral curves independent of the angle α (in the near-axis approximation). As viscosity may be stabilizing or destabilizing, the relevance of inviscid criteria is questionable for this problem. Also questionable is the validity of the quasi-static assumption, as the timescale for roll growth appears to be comparable with the period of oscillation. Rayleigh-type criteria have been developed for oscillatory shear layers without cell rotation or curvature of the flow (Kerczek & Davis 1974). This study does not appear to be applicable to the oscillating cell.

Most studies of oscillatory Stokes flows have concentrated on the regime where the Stokes-layer thickness, δ_S, is considerably smaller than the y-distance to any other wall. In our study, we have focused on the regime where $2\pi\delta_S/d$ and $4\pi\xi/d$ are order 1 (as is shown in figure 4). The limit of small δ_S/d would occur for much larger values of Φ than we have investigated.

Unidirectional flows influenced by rotation may also give rise to roll-type structures, as cited in §1. The roll orientation parallel to the basic-state flow and some of the initial bifurcations we report are similar to the large-aspect-ratio study of Alfredsson & Persson (1989). The generalized Rayleigh discriminant of Mutabazi, Normand & Wesfried (1992) would yield an instantaneous stability criterion independent of the maximal angle α, and is thus not a relevant criterion for this oscillating cell.

We have already emphasized that the roll-axis orientation is parallel to the basic-state velocity, as is the case for rolls in Taylor–Couette flow. This is in contrast to the most unstable roll-type mode of the Kelvin–Helmholtz instability, where the roll axes are perpendicular to the basic-state velocity. Apparently, when a potentially destabilizing body force is present (not present for the Kelvin–Helmholtz case), the roll orientation parallel to the flow is preferred. In this study, centrifugal, Coriolis, Euler, and inertial forces are potentially destabilizing; Hall maintains that the Coriolis force is responsible for the roll-type instability. Rayleigh–Bénard convection with shear imposed also favours roll development parallel to the flow: the body force is from buoyancy. We have been unable to find a general theory regarding such roll orientation preferences in the literature.

Most of the phenomena described here exhibit features in common with numerous flow regimes. These include roll onset, secondary wavy instabilities, wavelength adjustment by propagation of defects, front propagation, hysteresis, and coherent structure in turbulence. An increase in equilibrium wavelengths with increased forcing has also been observed in a variety of flows.

5.3. *Some possible extensions of this study*

A number of interesting extensions of this experiment are possible. We have noted that the location of the neutral curves are relatively insensitive to the aspect ratios (A_x and A_z of §2.1). For very large aspect ratios, we expect that the neutral curves will remain the same, but that the roll pattern may weaken far from the axis. If $A_x = 1$, we do not expect any roll development, owing to symmetry considerations.

Roll development appears to be crucially dependent upon the oscillation of the cell. However, rolls do develop with a superposition of oscillations and mean rotation ($\theta = at - \alpha \cos \omega t$). If $a \geqslant \alpha\omega$, the cell always rotates in the same direction. Even so, rolls still develop. An experimental study along these lines may reveal how mean flow and mean Coriolis forces affect roll development.

Consider a long cylindrical tube of radius R. If such a tube is subjected to oscillatory rotation, with the rotational axis perpendicular to the axis of the cylinder, a single strong roll develops. (This roughly corresponds to $L_z = R$ and $d = R$.) An interesting feature of this configuration is that, depending on initial conditions, we have sometimes observed a section of the tube with a laminar roll turning in one direction, in contact with a laminar roll turning in the opposite direction. The front (located at some value of x) between these two rolls is typically turbulent. We have not examined the regime diagram for this configuration, nor have we characterized the motion of the front that is sometimes present.

6. Concluding remarks

Fluid instabilities exhibit symmetry breaking of collective modes throughout the initial bifurcations from some initial state. If the basic state is independent of time, a linear stability analysis may be capable of capturing the neutral curve for the first symmetry-breaking mode, so long as the bifurcation is supercritical. Subcritical instabilities are not well described by linear theory, as they arise from finite-amplitude disturbances. A typical scenario for the initial bifurcations involves onset, growth governed by nonlinear processes, and successively more complicated (and less symmetric) modes. The linear stability analysis of the basic state invokes Floquet theory in a similar way as did Seminara & Hall (1976). As noted above, Hall (1994) has performed a linear stability analysis in the near-axis approximation.

A simple device may demonstrate the entire sequence of bifurcations, from the initial onset of low-dimensional structure, to coherent structures in turbulence. An oscillatory shear flow provides a basic state from which roll-type instabilities occur. The nonlinear growth of the rolls exhibits wavy instabilities of the rolls. Many of the features observed appear similar to the initial bifurcations in Taylor–Couette flow.

We would like to acknowledge helpful discussions with F. H. Busse, Stephan Fauve, Philip Hall, Robert Kelly, Arne Pearlstein, Bernard Perrin, Neil Ribe, Ronald Smith, George Veronis, Wenjie Zhao, and the group at the 1992 Summer Study Program in Geophysical Fluid Dynamics at Woods Hole. We thank Patrick Tabeling for providing a compact form for the derivation of the basic-state shear flow. This work was supported by CNRS and (for E.W.B.) a Joliot-Curie bourse administered by the French Commissariat à l'Energie Atomique. Additional support was provided by the US National Science Foundation (EAR-8721027 and EAR-8916241). The initial experimental results were presented at a meeting of the Division of Fluid Dynamics of The American Physical Society (Bolton & Maurer 1987).

REFERENCES

AKHAVAN, R., KAMM, R. D. & SHAPIRO, A. H. 1991*a* An investigation of transition to turbulence in bounded oscillatory Stokes flows. Part 1. Experiments. *J. Fluid Mech.* **225**, 395–422.

AKHAVAN, R., KAMM, R. D. & SHAPIRO, A. H. 1991*b* An investigation of transition to turbulence in bounded oscillatory Stokes flows. Part 2. Numerical simulations. *J. Fluid Mech.* **225**, 423–444.

ALFREDSSON, P. H. & PERSSON, H. 1989 Instabilities in channel flow with system rotation. *J. Fluid Mech.* **202**, 543–557.

BOLTON, E. W. & MAURER, J. 1987 A new roll-type instability is an oscillating fluid plane. *Bull. Am. Phys. Soc.* **33**, 2097.

COLES, D. 1965 Transition in circular Couette flow. *J. Fluid Mech.* **21**, 385–425.

DAVIS, S. H. 1976 The stability of time-periodic flows. *Ann. Rev. Fluid Mech.* **8**, 57–74.

DRAZIN, P. G. & REID, W. H. 1981 *Hydrodynamic Stability*. Cambridge University Press.

FENSTERMACHER, P. R., SWINNEY, H. L. & GOLLUB, J. P. 1979 Dynamical instabilities and the transition to chaotic Taylor vortex flow. *J. Fluid Mech.* **94**, 103–129.

HALL, P. 1978 The linear stability of flat Stokes layers. *Proc. R. Soc. Lond.* A **359**, 151–166.

HALL, P. 1981 Centrifugal instability of a Stokes layer: subharmonic destabilization of the Taylor vortex mode. *J. Fluid Mech.* **105**, 523–530.

HALL, P. 1994 On the instability of the flow in an oscillating tank of fluid. *J. Fluid Mech.* **268**, 315–331.

HART, J. E. 1971 Instability and secondary motion in a rotating channel flow. *J. Fluid Mech.* **45**, 341–351.

IOOSS, G. & JOSEPH, D. D. 1980 *Elementary Stability and Bifurcation Theory*. Springer.

KERCZEK, C. VON & DAVIS, S. H. 1974 Linear stability theory of oscillatory Stokes layers. *J. Fluid Mech.* **62**, 753–773.

KHESHGI, H. S. & SCRIVEN, L. E. 1985 Viscous flow through a rotating square channel. *Phys. Fluids* **28**, 2968–2979.

KOSCHMIEDER, E. L. 1979 Turbulent Taylor vortex flow. *J. Fluid Mech.* **93**, 515–527.

LANCZOS, C. 1970 *The Variational Principles of Mechanics*, 4th edn. University of Toronto Press.

LEZIUS, D. K. & JOHNSTON, J. P. 1976 Roll-cell instabilities in rotating laminar and turbulent channel flows. *J. Fluid Mech.* **77**, 153–175.

MUTABAZI, I., NORMAND, C. & WESFREID, J. E. 1992 Gap size effects on centrifugally and rotationally driven instabilities. *Phys. Fluids* A **4**, 1199–1205.

PARK, K., BARENGHI, C. & DONNELLY, R. J. 1980 Subharmonic destabilization of Taylor vortices near an oscillating cylinder. *Phys. Lett.* **78A**, 152–154.

SEMINARA, G. & HALL, P. 1976 Centrifugal instability of a Stokes layer: linear theory. *Proc. R. Soc. Lond.* A **350**, 299–316.

SPEZIALE, C. G. 1982 Numerical study of viscous flow in rotating rectangular ducts. *J. Fluid Mech.* **122**, 251–271.

WASHBURN, E. W. (Ed.) 1928 *International Critical Tables of Numerical Data, Physics, Chemistry and Technology*. McGraw-Hill.

WEAST, R. C. (Ed.) 1971 *Handbook of Chemistry and Physics*. The Chemical Rubber Co.